Research Article

Correlation of photocatalytic activity and defects generated in Ca^{2+}-based heterojunctions

Ubirajara Coleto Jr[1,2] · Rafael A. C. Amoresi[3] · Chrystopher A. M. Pereira[1] · Bruna W. Schmidt[1] · Isabela M. Iani[1] · Alexandre Z. Simões[3] · Elias S. Monteiro[1] · Elson Longo[4] · Maria A. Zaghete[1] · Leinig A. Perazolli[1]

Received: 10 July 2020 / Accepted: 12 October 2020 / Published online: 21 October 2020

Abstract
In this work a new semiconductor based on calcium heterojunction ($CaO/CaTiO_3$) was evaluated to the optical properties correlated to crystalline lattice defects. The heterojunctions of the semiconductor were prepared by the sol–gel route and its formation was confirmed by the intimate contact interface between crystalline phases. Morphology and elemental composition of the nanometric heterojunction were evaluated. Chemical environment and composition of the surface were used to determine the oxidation state of the material constituents. The electronic structure was evaluated and the relationship among band gap energy, photoluminescent emission energy, and photocatalytic activity of the materials was demonstrated. Oxygen vacancies located on the surface promoted photoluminescent spectra emission in the green wavelength, making them more photoactive than those defects that emitted in the red region. The use of active species scavenger indicated that the photogenerated species with the greatest photocatalytic action was the superoxide radical. This study has developed calcium heterojunctions for application as photocatalysts, demonstrating the importance of the defects generated in the production of heterojunctions and the activity of photogenerated species, studied using scavengers.

Keywords Heterojunctions · Structural defects · Oxygen vacancies · Photocatalysis · Scavenger

1 Introduction

It is extremely important for new devices to evaluate how the defects present in a crystalline lattice of semiconductor oxides influence the most diverse properties (electrical, optical, sensor, magnetic). Studies have shown that the composition of perovskite doping applied to the solar cell improves its performance due to the trapping of defects on the surface of the materials [1, 2]. In the same sense, materials applied to the anti-reflective coating have shown their performance is related not only to the composition but also to the type of defect generated in the structure [3–5]. Among the numerous applications, the photocatalytic also has features closely related to the presence of defects. In the fight against increasing water pollution, environmental remediation by photocatalysis has been a focus of the scientific community [6–8]. Highly photoactive materials that act in water decontamination have structural defects such as oxygen vacancies [9–13]. One way to generate structural defects is through the

Electronic supplementary material The online version of this article (https://doi.org/10.1007/s42452-020-03662-6) contains supplementary material, which is available to authorized users.

✉ Ubirajara Coleto Jr , biracoleto@ifsp.edu.br | [1]LIEC - Chemistry Institute, São Paulo State University - UNESP, Araraquara, SP 14800-060, Brazil. [2]Department of Chemistry, Federal Institute of São Paulo - IFSP, Catanduva, SP 15808-305, Brazil. [3]Faculty of Engineering of Guaratinguetá, UNESP, Guaratinguetá, SP 12516-410, Brazil. [4]LIEC - Department of Chemistry, São Carlos Federal University - UFSCar, São Carlos, SP 13565-905, Brazil.

formation of heterojunctions [14, 15] whose interfaces act as regions of charge carriers that alter the electrical, optical and magnetic properties of the material according to the band structures of the present phases [16]. Composition and modification are another strategy to the design of the photocatalysts with higher reactivity of active sites and the desired surface, and thus reducing the charge carriers recombination and enhancing the photocatalytic activity [17, 18]. The strategies of obtaining heterojunctions for the effective separation, transfer and suppression of the charges combination are in several applications to obtain clean and sustainable energy sources. Oxygen and hydrogen evolution reaction for the purpose of water splitting are reactions totally dependent on the electronic structure and the behavior of the charge carriers present in the materials interface region [19–21]. Such properties that depend on the semiconductors photoelectrochemical behavior show improvements due to synergistic effects of the interface and oxygen vacancies obtained in these materials [21].

For large-scale application, it is necessary that the photocatalyst be abundant, easily obtainable and inexpensive; one such material that has been studied for such characteristics is CaO [11, 22–25]. Such compounds have been doped with metal ions based on their heterostructures [11, 26–30]. During CaO synthesis, other phases, such as hydroxide ($Ca(OH)_2$) and carbonate ($CaCO_3$), which also exhibit significant photocatalytic activity, [11, 22–24] can be detected. Pure, doped or heterostructured CaO has high photocatalytic versatility and has been studied in the application of dye discoloration [11, 22–24], biodiesel production via palm oil transesterification [29] biodiesel production via free fatty acid esterification [26, 28], synthesis of organic compounds [28], antibiotic degradation [27], ammonia degradation [31] and palm oil degradation [30].

$CaTiO_3$ is a material that can be used to form heterostructures with CaO, an n-type semiconductor [32] with an ABO_3 perovskite structure, with Ti–O terminations and a band gap of 3.5 eV [32, 33]. $CaTiO_3$ has also been prepared for photocatalytic purposes with the addition of lattice and surface modifiers, e.g., Au decoration. In this compound, Rhodamine B (RhB) was 99.6% degraded under simulated solar irradiation during 120 min of photocatalytic reaction due to efficient separation of the photoexcited electron/hole (e^-/h^+) pairs, owing to electron transfer from the $CaTiO_3$ to the Au [34].

Compared to $CaTiO_3/Eu^{3+}$ without Ni^0, Eu^{3+}/Ni^0-doped $CaTiO_3$ showed a higher photocatalytic activity for toluene degradation attributed to the lower photocatalyst band gap energy value [35], that is, a direct relationship with the defects present in the material structure. The $CaTiO_3/TiO_2$ heterojunction was used for photocatalytic CO_2 reduction, exhibiting five times more efficiency compared to undoped TiO_2. This result was attributed to crystal band structures, efficient separation of e^-/h^+ pairs, and the surface basicity of the $CaTiO_3/TiO_2$ composites that facilitated CO_2 adsorption and activation [36]. CdSe-modified $CaTiO_3$ nanocomposites and g-C_3N_4 have been reported as photocatalysts in hydrogen production [37, 38]. As an extension of our previous work [9–11], in this study, we have developed calcium heterojunctions demonstrating the importance of the defects generated in the formation of heterojunctions and the activity of photogenerated species, studied using scavengers.

2 Experimental

2.1 Heterojunction production by sol–gel method

For the production of Ca-based heterojunctions, titanium isopropoxide (Sigma-Aldrich, 97%) and acetic acid (Qhemis, 99.7%) were used in a 1:4 molar ratio. The acid was added to the titanium isopropoxide at a temperature of 100 °C and remained under constant stirring for 3 h. The titanium acetate formed was standardized, and the number of moles of Ti^{4+}/g of titanium acetate was calculated. Concomitantly, a suspension of CaO (Êxodo, 95%) and isopropanol (Vetec, 99.5%) was obtained using a 1:10 molar ratio. This suspension was added to the titanium acetate solution. The concentration of titanium acetate was calculated to generate heterojunctions with 0.25%, 0.50%, 2.0%, 10.0% and 50.0% by weight of the $CaTiO_3$ (CTO) in the CaO matrix, resulting in samples Ca + 0.25%CTO, Ca + 0.5%CTO, Ca + 2%CTO, Ca + 10%CTO and Ca + 50%CTO, respectively. The solid formed was dried at 150 °C for 12 h in a muffle furnace under air flow. Thereafter, the samples were heat treated at 350 °C for 4 h to remove organic matter, followed by treatment at 500 °C for 4 h. All heat treatments were done with air flow. The CaO used was a commercial reagent, Exôdo®, 95%.

2.2 Heterojunctions characterization

The materials were investigated by Thermogravimetry and Differential Thermal Analysis (TG/DTA) in NETZSCH® equipment. The samples were heated to 1000 °C at a rate of 10 °C/min using a nitrogen atmosphere. X-ray Diffraction (XRD) analyses were obtained using a Rigaku® diffractometer, model RINT2000. Measurements were made with a monochromatic X-ray beam by copper Kα radiation (50 kV, 120 mA) with emission wavelengths of 1.54 Å in increments of $\Delta 2\theta = 0.02°$. UV/Vis/NIR Diffuse Reflectance Spectroscopy (UV/Vis/NIR DRS) characterization was performed using the Perkin Elmer® Lambda 1050 model UV–Vis-NIR absorption spectrophotometer with an integrating sphere

150 mm in diameter with InGaAs (NIR) and PMT (UV/Vis) detectors. Analyses were performed in the 200–800 nm spectral range in diffuse reflectance mode. The spectra were used to calculate the band gap energy of the materials using the Kubelka–Munk algorithm.

Photoluminescence (PL) characterization of samples was performed using a 325 nm laser, and the spectra were recorded in the range of 350 nm to 850 nm. Field Emission Scanning Electron Microscopy (FE-SEM) and Energy Dispersion Spectroscopy (EDS) using FEG-MEV JEOL® Model 7500F equipment with secondary electron detectors was used to illustrate the morphology and indicate the qualitative chemical composition. High Resolution Transmission Electron Microscopy (HRTEM) with a FEI TECNAI G^2 F20 HRTEM® transmission electron microscope was used to identify the structures of the crystalline phases that formed the heterojunction as well as to illustrate the interface regions and short range defects. The Ca + 0.25%CTO (w/w) and Ca + 10%CTO (w/w) samples were characterized by X-ray Excited Photoelectron Spectroscopy (XPS) using a krypton laser (Coherent Innova 200) as the excitation source with a wavelength of 350 nm on Scientia Omicron® equipment with $Al_{K\alpha}$ X-ray source.

2.3 Photoactivity of catalysts for discoloration of RhB

To evaluate the photocatalytic activity of the samples, 700 mL of 10^{-5} mol/L RhB dye aqueous solution was sonicated for 20 min in a dark room. For the light source, the photocatalytic process included a UV lamp (λ_{max} = 254 nm, 11 W, Osram, Puritec HNS 2G7) placed inside a quartz tube inside the reactor. Constant suspension agitation and air bubbling were used. Aliquots were collected from the photocatalytic reaction at several points in the reaction, centrifuged and analyzed on a Perkin Elmer® Lambda 1050 spectrophotometer. Photocatalytic efficiency was measured by the percentage of discoloration of Rhodamine B solution, according to Eq. (1) below, and RhB photodiscoloration half-life ($t_{1/2}$) was calculated using Eq. (2) below:

$$\%D = \frac{C_0 - C_t}{C_0} \cdot 100 \quad (1)$$

$$t_{1/2} = \frac{\ln 2}{k} \quad (2)$$

where: % D = percentage of discoloration, C_0 = Dye concentration at time zero, C_t = Dye concentration at time t, $t_{1/2}$ = half-life, k = reaction rate.

To study the reusability and stability of the photocatalysts, the photocatalysts was separated from the suspension by centrifugation, calcined at 500 °C, analyzed by XRD, weighed and reused in the photocatalysis. Three cycles of photocatalysis were performed using Ca + 0.25%CTO as a photocatalyst.

To study the mechanism of action of the photocatalysts, CaO, $CaTiO_3$, and Ca + 0.25%CTO were used under the same conditions described above, but scavengers was added before the ultrasound. It was used as an electronic hole scavenger (h^+) 1 mmol/ disodium EDTA, as a superoxide radical scavenger ($O_2^{\cdot-}$) 1 mmol/L p-benzoquinone, and as a hydroxyl radical scavenger ($OH^{\cdot}$) 200 mmol/L of isopropanol.

3 Results and discussion

3.1 Structural, morphological and electronic characterization

X-ray diffraction pattern profiles of the heterojunctions are shown in Fig. 1a. Peaks were attributed to CaO, $CaCO_3$, $Ca(OH)_2$, and $CaTiO_3$ phases, as identified by similarity to JCPDS standards no 60199, 20179, 73467, and 74213. The addition of up to 2% of Ti ions to the CaO did not allow for identification of the perovskite phase of $CaTiO_3$. In turn, the XRD of the Ca + 10%$CaTiO_3$, Fig. 1b, indicated the presence of a two theta peaks at 32.7 relative to the $CaTiO_3$ plane (112).

The Ca + 50%CTO showed peaks at 32.8, 40.5, 47.3, 58.7, 69.0, and 78.6 degrees, related to the $CaTiO_3$ phase. The peak intensities of samples containing 10% and 50% of $CaTiO_3$ were different, demonstrating that the concentration of the perovskite phase changed for each heterojunction. Results from TG/DTA, Fig. S-1, and Table S-1 demonstrated the constitution of the materials, in which the $CaTiO_3$ phase formation increased proportionally to the Ti ions added in the synthesis.

Heterojunction formation was verified by HRTEM analysis with the Ca + 10%CTO sample, as seen in Fig. 2. The sample had distances of 2.78 Å of the (111) CaO plane, 3.43 Å of the (111) $CaTiO_3$ plane, 3.86 Å of the (012) $CaCO_3$ plane, and 3.11 Å of the (111) $Ca(OH)_2$ plane. This result showed the intimate contact interface formation of a quaternary heterojunction [39], wherein the structures CaO cubic, $CaTiO_3$ orthorhombic, and $CaCO_3$, $Ca(OH)_2$ trigonal were the constituents. The formation of this heterojunction was thermodynamically favorable since the lattice mismatches were similar. For instance, consider the CaO-cubic/$CaCO_3$-trigonal system, in which the lattice mismatch was 4% (a_{CaO} = 4.812 Å and a_{CaCO3} = 4.994 Å) or the $CaCO_3$-trigonal/$Ca(OH)_2$-trigonal system, with a mismatch of 2% (a_{CaCO3} = 4.994 Å and $c_{Ca(OH)2}$ = 4.911 Å). FE-SEM analysis, Fig. 3, shows that the CaO had a micrometric size particle and CaO/$CaTiO_3$/$CaCO_3$/$Ca(OH)_2$ heterojunctions

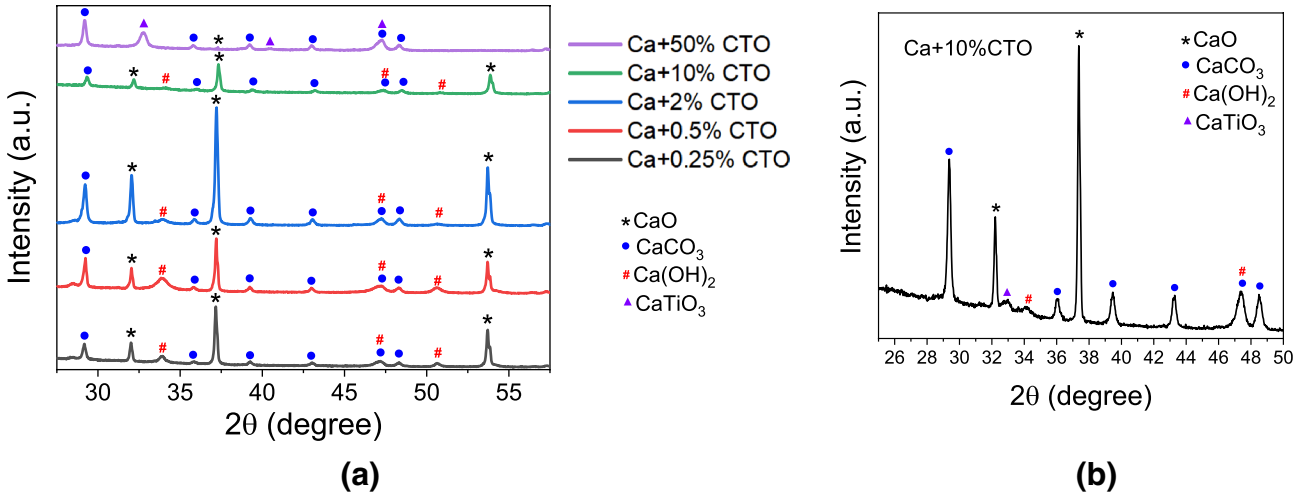

Fig. 1 X-ray diffraction of $CaO/CaTiO_3/CaCO_3/Ca(OH)_2$ heterojunctions

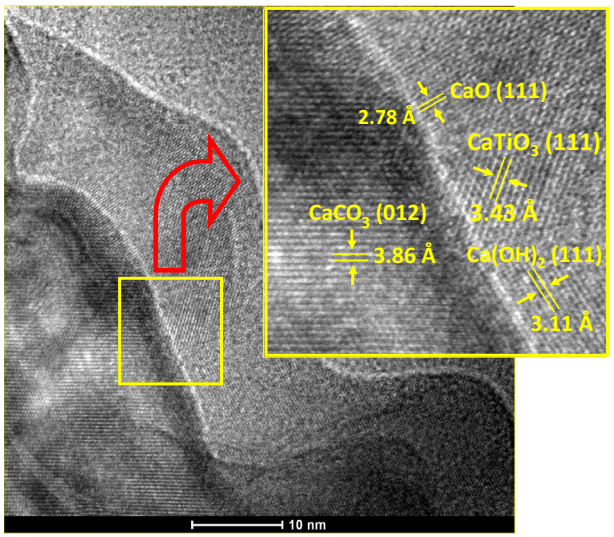

Fig. 2 HRTEM of Ca + 10%CTO heterojunction interface with expansion of the central region

had nanometric, spherical, and agglomerate grains. It was found that the increase in $CaTiO_3$ concentration resulted in a decrease in average particle size, Table 1. EDS spectra of the Ca + 10%CTO sample, Fig. 3e, revealed the distribution composition of the elements presented in the heterojunction. These results showed peaks related to the O, Ca, and Ti at 0.52 keV, 3.69 keV, and 4.51 keV at Kα, respectively, which represented sample compositions, and at Si, the Kα peak at 1.74 keV represented the sample holder for analysis. The wide region, region 1, illustrated high intensity peaks related to Ca and O, which referred to the sample matrix, and a low intensity of Ti peak, which referred to the heterojunction. Analyzing specific regions of the sample, points 2 and 3 showed grains formed exclusively by Ca, without Ti composition, and point 2 showed grains rich in Ti, with a Ti peak of intensity higher than those measured in a large region of the sample, point 3. It was concluded that $CaTiO_3$ inserted in the sample was not a solid solution, which was in agreement with the formation of the heterojunction.

Electronically, the samples were characterized by diffuse reflectance and photoluminescent spectroscopy, as illustrated in Figs. 4 and 5. Results of diffuse reflectance spectra (see Fig. 4 and Table 2) to the CaO, $CaTiO_3$, and $CaO/CaTiO_3/CaCO_3/Ca(OH)_2$ samples showed a direct band gap energy by the Kubelka–Munk algorithm [32, 33, 40–42]. Heterojunctions showed lower band gap energy with increasing $CaTiO_3$ concentration. This was due to the increasing perovskite concentration and decreased dielectric $Ca(OH)_2$ concentration [11], which promoted decreased band gap energy.

Figure 5 shows the PL emission spectra of CaO, $CaTiO_3$, and the heterojunctions. It can be observed from the CaO emission spectrum that the band-to-band recombination, formed by an electron photoexcited in the conduction band (CB) and an electronic hole in the valence band (VB)–recombination, occurred at different energy levels in the band gap region. In this sample, the highest emission intensity occurred in three main regions (410 nm, 570 nm, and 780 nm). In the heterojunction sample, the PL intensity decreased, which induced suppression of the band-to-band recombination. Another characteristic of $CaO/CaTiO_3/CaCO_3/Ca(OH)_2$ heterojunctions was the narrower spectra compared to CaO, with maximum intensity at approximately 550 nm. $CaTiO_3$, as well as the heterojunctions containing a higher $CaTiO_3$ concentration, had a low intensity of band-to-band recombination, a characteristic

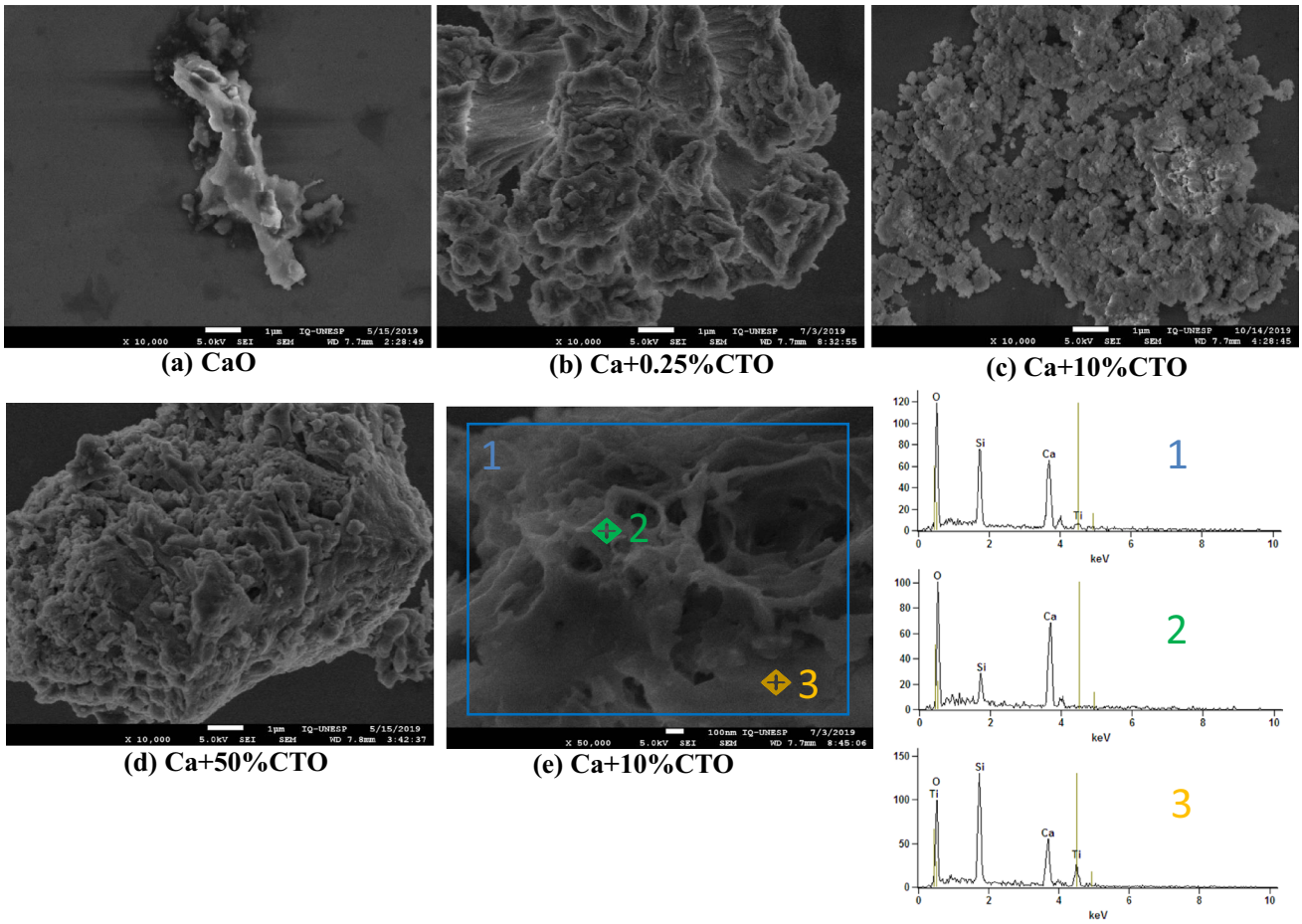

Fig. 3 FE-SEM micrographs of the samples: **a** CaO; **b** Ca + 0.25%CTO; **c** Ca + 10%CTO; **d** Ca + 50%CTO; and **e** FE-SEM–EDS analysis of Ca + 10%CTO heterojunction

Table 1 Average particle size of samples

Samples	Average particle size (nm)
CaO	400
Ca + 0.25%CTO	390
Ca + 10%CTO	200
Ca + 50%CTO	180

also found in the $SrTiO_3$ [11]. Deconvolution of PL spectra, Fig. 6, was performed for a more detailed analysis of the emission regions, and, in follow-up, the types of defects present in the pure and heterojunctions samples are discussed.

CaO showed five emission bands, due to different types of intrinsic structural defects of the material, with energy ranging from 3.02 eV (violet region, 411 nm) up to 1.62 eV (infrared region, 764 nm). The violet region band indicated direct recombination of an e^-/h^+ pair between the CB and VB. In addition, the emission in this region is a characteristic of material defects, mainly characteristic of the presence of oxygen vacancies (V_O^x, $V_O^{\cdot}$, $V_O^{\cdot\cdot}$). In which the superscripts '^{x}', '$^{\cdot}$', and '$^{\cdot\cdot}$', indicate types of neutral, mono, and double ionized vacancies, respectively [9–11, 43, 44]. The band in the blue region indicated a $V_O^{\cdot}$ type and bands in the green and red region referred to $V_O^{\cdot\cdot}$ type vacancies [43, 45]. The infrared region band was caused by distortion of the crystal lattice by the formation of the heterojunction [9–11, 43, 44, 46, 47]. The photoluminescent deconvolution spectrum of $CaTiO_3$ showed green/red and infrared bands, which represented double-ionized oxygen vacancies and crystal lattice distortion, respectively. The $CaO/CaTiO_3/CaCO_3/Ca(OH)_2$ heterojunctions spectra showed two bands, one in the green and one in the red region. Heterojunctions with spectra in the green/red region are indicative of the presence of double-ionized oxygen vacancies that acted as electron receptors [9–11, 43, 44]. The increase in $CaTiO_3$ concentration in the CaO matrix changed the

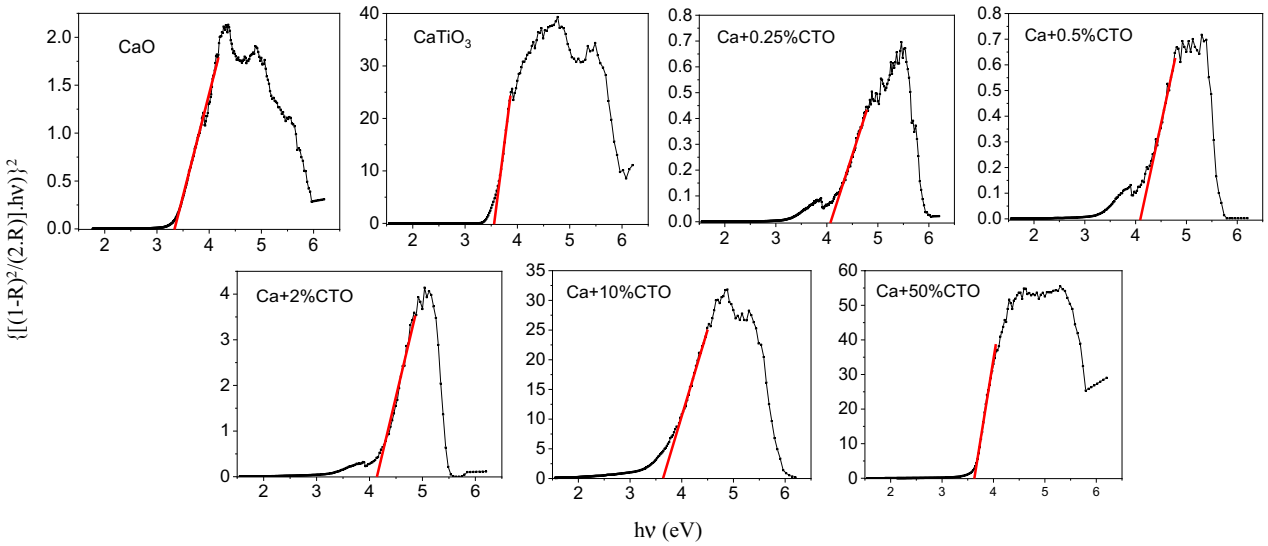

Fig. 4 Direct band gap energy graphs by Kubelka–Munk algorithm obtained by diffuse reflectance of the CaO, $CaTiO_3$, and CaO/$CaTiO_3$/$CaCO_3$/$Ca(OH)_2$ samples

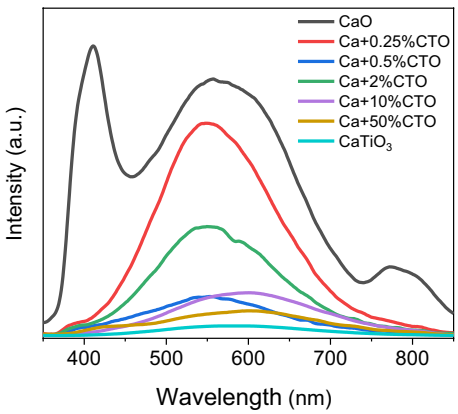

Fig. 5 Photoluminescence spectra obtained from CaO and $CaTiO_3$ samples and CaO/$CaTiO_3$/$CaCO_3$/$Ca(OH)_2$ heterojunctions

Table 2 Direct band gap energy of the studied materials

Samples	E_{gap} (eV)
CaO	3.3
$CaTiO_3$	3.6
Ca + 0.25%CTO	4.1
Ca + 0.5%CTO	4.1
Ca + 2%CTO	4.1
Ca + 10%CTO	3.6
Ca + 50%CTO	3.6

main emission region, resulting in an increase in the red region emission band.

The chemical environments of the Ca + 0.25%CTO and Ca + 10%CTO heterojunctions were investigated by XPS Fig. 7. Survey spectra of Ca + 0.25%CTO and Ca + 10%CTO heterojunctions are shown in Fig. 7a, f. Ca and Ti elements could be detected in the spectra at peaks 2p (~347 eV and ~457 eV). O 1 s is present in the region of 531 eV, and the C 1 s appears at approximately 285 eV. According to the results, the Ca 2p peak indicated the +2 oxidation state and the Ti 2p peak indicated the +4 oxidation state, as seen in Fig. 7b, c, g, h, respectively. This indicated that obtaining heterojunction with low or high $CaTiO_3$ concentration did not alter the oxidation state of the metal ions present in the crystal lattice. The presence of carbonate on the surface was confirmed by C 1 s peaks at 289.3 eV [48, 49], (Fig. 7d, i). The O 1 s peak was deconvoluted into two peaks (Fig. 7e, j): one with a binding energy of approximately 531.1 eV, reflecting the metal–oxygen bonding of the crystal lattice (Ca-O and Ti–O) [28, 50] and the presence of hydroxyls ($Ca(OH)_2$ and -OH terminations) [51], and a peak at approximately 532.5 eV, reflecting the carbon–oxygen bonding (–CO_3) [52, 53] and structural defects as oxygen vacancy [52, 54]. Thus, the peak at approximately 532.5 eV confirms the presence of oxygen vacancies, also verified by the PL analysis. O 1 s deconvolution to the Ca + 0.25%CTO heterojunction showed the peak relative to $CaCO_3$ and oxygen vacancies (532.7 eV) (Fig. 7e), with 22.9% of the peak area, while in the Ca + 10%CTO heterojunction, this value decreased to 15.9%. The Ca + 10%CTO sample would be expected to have the highest peak area (~532.6 eV) as it has the highest proportion of carbonate (Fig. S1—42.5%). However, this result demonstrated that the highest peak area (~532.6 eV) of the Ca + 0.25%CTO sample reflected the oxygen vacancies found on the material surface. As the Ca + 0.25%CTO heterojunction presented a higher PL

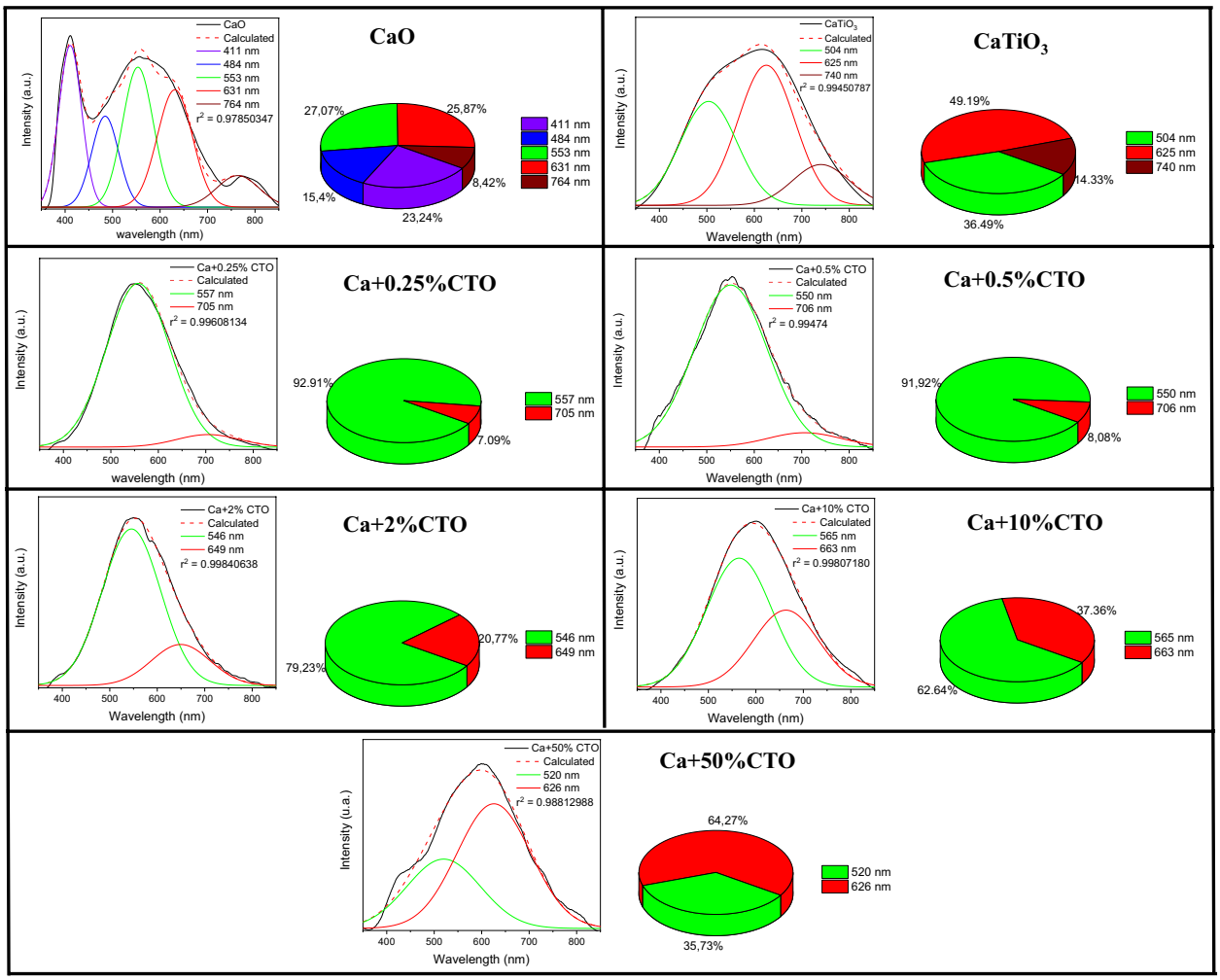

Fig. 6 Deconvolution of CaO, $CaTiO_3$ photoluminescent spectra and CaO/$CaTiO_3$/$CaCO_3$/$Ca(OH)_2$ heterojunctions

emission in the green region (Fig. 6), and this emission was mainly related to defects of the oxygen vacancy type (Fig. 7e), one could deduce the types of defects present in the crystalline structure clusters, Eqs. 3–8:

$$\left[CaO_6\right]_o^x + \left[CaO_5\,V_o^x\right]_d \rightarrow \left[CaO_6\right]_o^{'} + \left[CaO_5\,V_o^{\cdot}\right]_d \quad (3)$$

$$\left[CaO_6\right]_o^x + \left[CaO_5\,V_o^{\cdot}\right]_d \rightarrow \left[CaO_6\right]_o^{'} + \left[CaO_5\,V_o^{\cdot\cdot}\right]_d \quad (4)$$

$$\left[TiO_6\right]_o^x + \left[TiO_5\,V_o^x\right]_d \rightarrow \left[TiO_6\right]_o^{'} + \left[TiO_5\,V_o^{\cdot}\right]_d \quad (5)$$

$$\left[TiO_6\right]_o^x + \left[TiO_5\,V_o^{\cdot}\right]_d \rightarrow \left[TiO_6\right]_o^{'} + \left[TiO_5\,V_o^{\cdot\cdot}\right]_d \quad (6)$$

$$\left[CaO_8\right]_o^x + \left[CaO_7\,V_o^x\right]_d \rightarrow \left[CaO_8\right]_o^{'} + \left[CaO_7\,V_o^{\cdot}\right]_d \quad (7)$$

$$\left[CaO_8\right]_o^x + \left[CaO_7\,V_o^{\cdot}\right]_d \rightarrow \left[CaO_8\right]_o^{'} + \left[CaO_7\,V_o^{\cdot\cdot}\right]_d \quad (8)$$

According to the Kroger Vink notations, the symbol V_O designates the oxygen vacancies, and the superscript x, dot (·), and comma (,), the vacancy types: neutral, hole, and electron, respectively. Equations (3) and (4) represent the formation of the mono- and double-ionized oxygen vacancy types in the $[CaO_6]$ clusters to CaO, $Ca(OH)_2$, and $CaCO_3$, and Eqs. (5) to (8), to $CaTiO_3$.

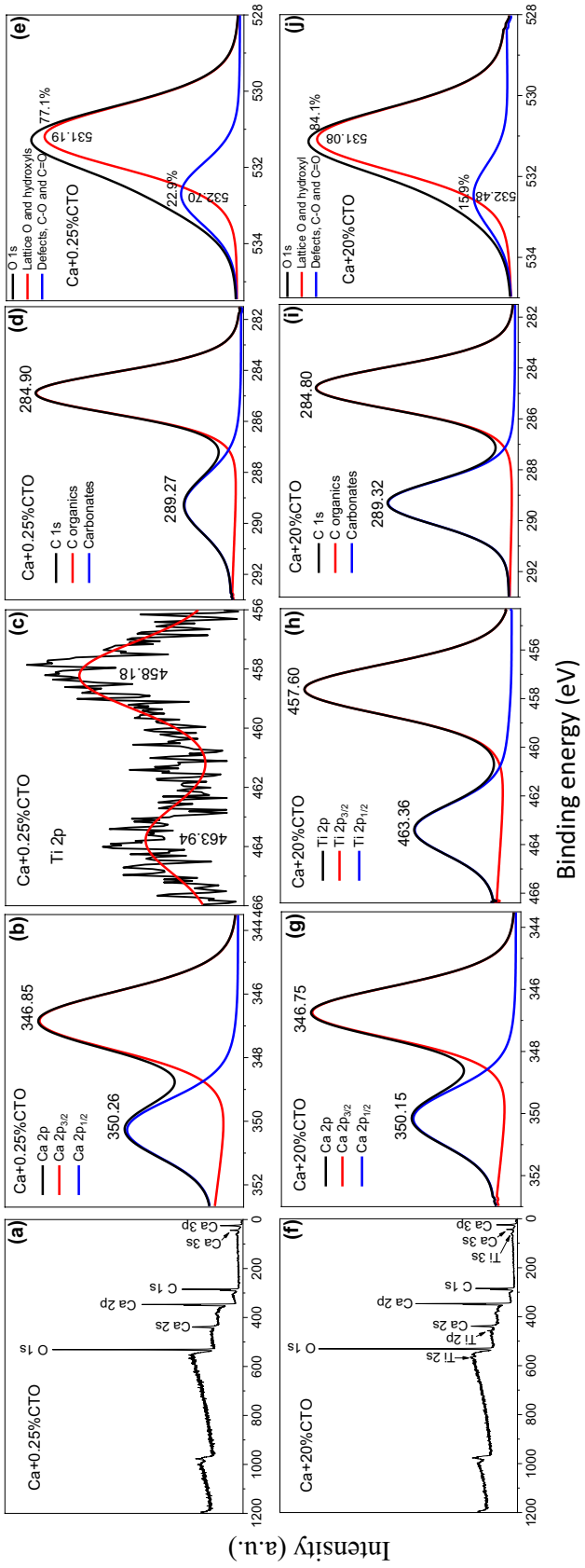

Fig. 7 XPS spectra: **a** survey spectrum Ca + 0.25%CTO sample; **b** spectrum of Ca 2p species of Ca + 0.25%CTO; **c** high resolution spectrum of Ti 2p species of Ca + 0.25%CTO; **d** spectrum of C 1 s species of Ca + 0.25%CTO; **e** spectrum of the O 1 s species of Ca + 0.25%CTO; **f** survey spectrum of Ca + 10%CTO sample; **g** Ca 2p species spectrum of Ca + 10% CTO; **h** spectrum of Ti 2p species of Ca + 10%CTO; **i** spectrum of C 1 s species of Ca + 10%CTO; **j** spectrum of O 1 s species of Ca + 10%CTO

3.2 Photoactivity of catalysts for RhB discoloration

Figure 8a illustrates the discoloration of RhB as a function of time and Fig. 8b illustrates the pseudo 1st order Langmuir–Hinshelwood kinetics graph, ln (A_0/A_t) as a function of time. From these data, we obtained the reaction rate constants (k) and calculated the half-life times ($t_{1/2}$) of the RhB photodiscoloration reaction, shown in Table 3.

The best photocatalytic activity was observed in RhB dye discoloration obtained with the Ca + 0.25%CTO sample, which had a calculated half-life of 38.5 min. The photocatalytic performance of the Ca + 0.25%CTO heterojunction investigated in this work was compared with the previous reports, as shown in the Table 4. It can be observed from these results that the heterojunction material obtained in this work has greater discoloration kinetics than its respective pure materials. The use of an electromagnetic radiation source with energy greater than or equal to band gap energy generated free electrons in the CB and electronic holes in the VB. Electrons could react with oxygen molecules to form superoxide radicals ($O_2^{\cdot-}$), just as electronic holes (h^+) could react with water or adsorbed hydroxyl ions to generate hydroxyl radicals ($OH^{\cdot}$). These three chemical species had photocatalytic action on RhB discoloration, according to Eqs. (9) to (16):

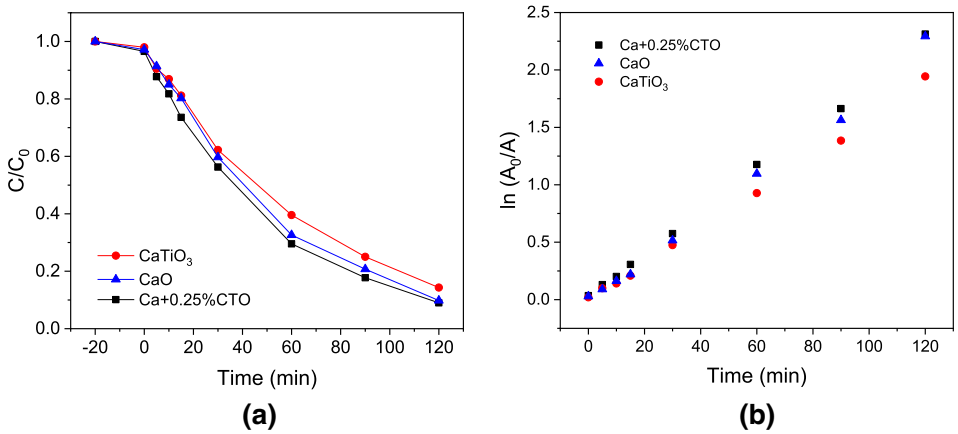

Fig. 8 Photocatalytic activity of CaO, $CaTiO_3$, and CaO/$CaTiO_3$/$CaCO_3$/$Ca(OH)_2$ heterojunction

Table 3 Photocatalysis data of CaO/$CaTiO_3$/$CaCO_3$/$Ca(OH)_2$ heterojunctions and their precursors

Samples	Discoloration in 120 min (%)	$k \times 10^{-2}$ (min^{-1})	$t_{1/2}$—calculated (min)	$t_{1/2}$—observed (min)
CaO	90.0	1.630	42.5	39.3
$CaTiO_3$	85.6	1.448	47.9	46.9
Ca + 0.25%CTO	90.1	1.799	38.5	37.4
Ca + 0.5%CTO	89.5	1.793	38.7	39.7
Ca + 2%CTO	86.8	1.530	45.3	44.8
Ca + 10%CTO	86.0	1.514	45.8	45.8
Ca + 50%CTO	41.2	0.395	175.5	–

Table 4 Photocatalytic performance of precursors and heterojunctions using UV light in previous reports

Photocatalyst	Synthesized method	Heat treatment (°C)	Target pollutant	$k \times 10^{-2}$ (min^{-1})	References
CaO	Polymeric precursor	1000	RhB	1.356	[11]
$CaTiO_3$	Roasting	1100	RhB	0.216	[64]
$Ca(OH)_2$	Calcination	800	Rh6G	*	[22]
$CaCO_3$	Precipitation	120	Rh6G	**	[22]
Ca + 0.25%CTO	Sol–Gel	500	RhB	1.799	This work

*50% efficiency after 250 min of photocatalysis

**13% efficiency after 250 min of photocatalysis

$$\text{Photocatalyst} + h\nu \rightarrow \text{Photocatalyst}\left(e^-_{CB} + h^+_{VB}\right) \quad (9)$$

$$\text{Photocatalyst}\left(e^-_{CB}\right) + O_2 \rightarrow \text{Photocatalyst} + O_2^{\cdot -} \quad (10)$$

$$\text{Photocatalyst}\left(h^+_{VB}\right) + H_2O_{ads} \rightarrow \text{Photocatalyst} + H^+ + OH^{\cdot}_{ads} \quad (11)$$

$$\text{Photocatalyst}\left(h^+_{VB}\right) + OH^-_{ads} \rightarrow \text{Photocatalyst} + OH^{\cdot}_{ads} \quad (12)$$

$$\text{Photocatalyst}\left(h^+_{VB}\right) + \text{RhB} \rightarrow \text{RhB}^{\cdot} + \text{RhB oxidation} \quad (13)$$

$$OH^{\cdot}_{ads} + \text{RhB} \rightarrow \text{RhB discoloration} \quad (14)$$

$$O_2^{\cdot -} + \text{RhB} \rightarrow \text{RhB discoloration} \quad (15)$$

$$e^-_{CB} + h^+_{VB} \rightarrow \text{heat} \quad (16)$$

The study of reuse and stability of the Ca + 0.25% CTO photocatalyst demonstrates that the photocatalyst is stable and can be reused, Fig. 9a. After three cycles of reuse, the photocatalyst remained active, with a reduction in its photoactivity of 11.6%. The good photocatalytic performance even after the 3 cycles can be attributed to the robustness of the photocatalyst that kept its crystalline constitution practically unchanged after reuse, Fig. 9b.

Scavenger tests were performed in order to compare the species with photocatalytic action in the most photoactive heterojunction. The photocatalytic activity of CaO, $CaTiO_3$, and Ca + 0.25%CTO samples when EDTA-Na_2 was used as an electronic hole (h^+) scavenger, isopropanol as a hydroxyl ($OH^{\cdot}$) radical scavenger and p-benzoquinone as a superoxide ($O_2^{\cdot -}$) radical scavenger, are shown in Fig. 10. The percentage indicated in the figure is related to 120 min of reaction time. Similar behaviors were found in the three samples (Table 5). In the three photocatalysts studied, it can be seen that by using EDTA-Na_2 and isopropanol, there was an approximate 40% reduction in dye discoloration, demonstrating that both h^+ and $OH^{\cdot}$ species had similar functions. Among the photogenerated species, the superoxide radical ($O_2^{\cdot -}$) showed the most relevant discoloration of approximately 27% after 120 min of reaction. Our results were in agreement with the study by Liu that also found that the most photoactive species was the superoxide radical [55], unlike the findings in other materials [10, 56–58].

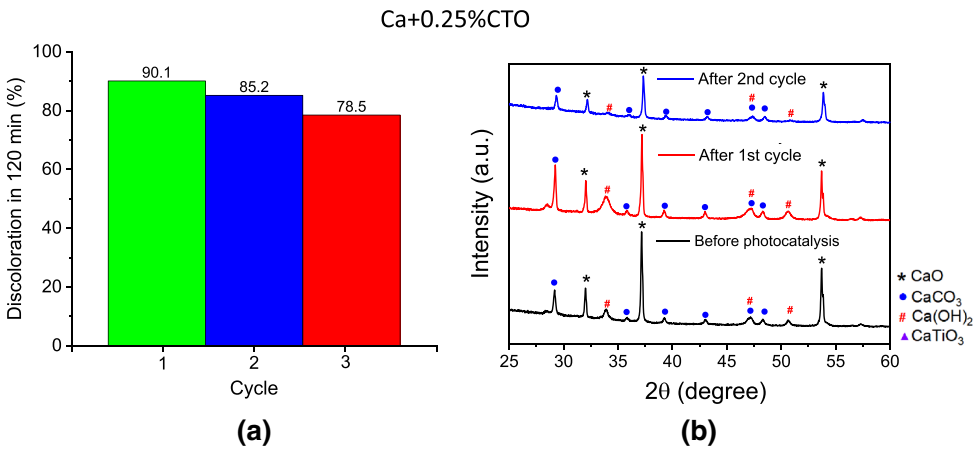

Fig. 9 Stability and Reusability of the heterojunction **a** Photocatalytic efficiency of the reused Ca + 0.25%CTO heterojunction for discoloration of the RhB dye for three cycles. **b** XRD analysis of the Ca + 0.25%CTO sample used in reuse

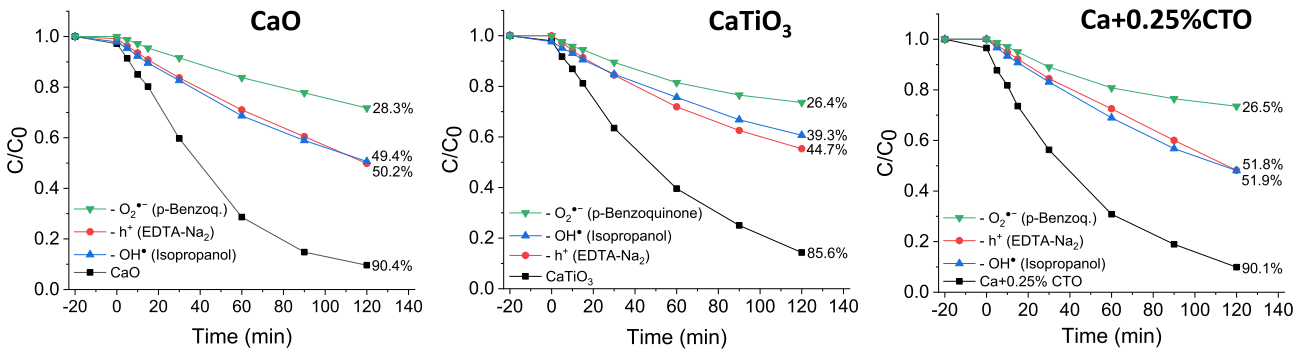

Fig. 10 Photocatalytic activity of CaO, $CaTiO_3$, and Ca + 0.25%CTO samples using scavengers

Table 5 RhB discoloration after 120 min under UV light using CaO, $CaTiO_3$ and Ca + 0.25%CTO samples with scavengers

	CaO (% disc.)	$CaTiO_3$ (% disc.)	Ca + 0.25%CTO (% disc.)
Without scavenger	90.0	85.6	90.1
(- h^+)	50.2	44.7	51.8
(- $OH^{\cdot}$)	49.4	39.3	51.9
(- $O_2^{\cdot -}$)	28.3	26.4	26.5

XRD and TG/DTA analyses indicated the presence of $Ca(OH)_2$ and $CaCO_3$, which were dielectric [59, 60]. Sanchez-Cantu verified that $Ca(OH)_2$, with a 5.69 eV band gap, presented high photoactivity attributed to the indirect sensitization of Rhodamine 6G dye. In this case, there was an electron transfer from the dye to the CB of the dielectric material, which interacted with the adsorbed species on the catalytic surface, producing radical species that acted on dye degradation [22]. Recently Pei et al. [61] has also correlated the catalytic efficiency of these materials with the presence of hydroxyl radical from calcium hydroxide. From the electrons injected into the photocatalyst, superoxide radicals formed that could, in turn, form hydroxyl radicals, according to Eqs. (17) to (23):

$$RhB + h\nu \rightarrow RhB^+ + e^- \tag{17}$$

$$e^- + \text{Photocatalyst} \rightarrow \text{Photocatalyst}\left(e^-_{CB}\right) \tag{18}$$

$$\text{Photocatalyst}\left(2e^-_{CB}\right) + O_2 + 2H^+ \rightarrow H_2O_2 + \text{Photocatalyst} \tag{19}$$

$$2O_2^{\cdot -} + 2H^+ \rightarrow H_2O_2 + O_2 \tag{20}$$

$$H_2O_2 + \text{Photocatalyst}\left(e^-_{CB}\right) \rightarrow OH^{\cdot} + OH^- + \text{Photocatalyst} \tag{21}$$

$$H_2O_2 + O_2^{\cdot -} \rightarrow OH^{\cdot} + OH^- + O_2 \tag{22}$$

$$H_2O_2 + h\nu \rightarrow 2OH^{\cdot} \tag{23}$$

P-Benzoquinone captures the photogenerated free electron, stabilizing it through resonance, as seen in Eq. (24), preventing the formation of superoxide and hydroxyl radicals. This electron capture is well elucidated in the described scavengers experiments, Fig. 10.

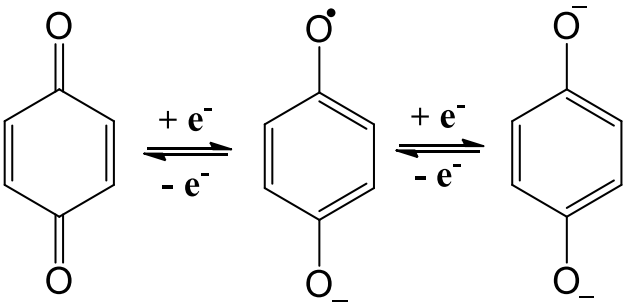

(24)

The CB and VB energy levels presented in scheme shown in the Fig. 11 were calculated using the empirical Eqs. (25) and (26) [62]:

$$E_{CB} = \chi - E_e - 0.5E_g \tag{25}$$

$$E_{VB} = E_{CB} + E_g \tag{26}$$

where E_{VB} and E_{CB} are the potentials in VB and CB, respectively. E_g is the energy gap calculated and E_e is the free electric energy versus hydrogen (4.5 eV) [62]. Finally, χ is the semiconductor electronegativity, 3.1815 eV for CaO [63] and 5.105 eV for $CaTiO_3$ [64]. Therefore, this is a type II heterojunction considering the alignment between the BV and CB of the materials.

The photocatalytic results indicated that formation of the heterojunction generated defects that acted as trappers of the charge carriers, increasing the recombination time of the photogenerated $e^-/h+$ pair. The TG/DTA results showed that there was no direct relationship between $CaCO_3$ and $Ca(OH)_2$ concentrations present in the heterojunctions and their photoactivities, indicating that there were other factors that influenced the photoactivity. The deconvolution of the PL spectra showed emission bands in the green and red region. Although both bands were generated by doubly-ionized oxygen vacancies, the increased red band resulted in a decrease in the photoactivity, shown in Table 6. Deconvolution spectrum PL to CaO resulted in five emission bands, indicating the possible paths of band-to-band recombination. Deconvolution spectrum PL to the heterojuntion showed only two emission bands, limiting the paths of recombination of the e^-/h^+ pair. Increasing the $CaTiO_3$ concentration in heterojunctions decreases the recombination that occurs in the highest energy (green) region, and increases recombination in the lowest energy (red) region. Therefore, photocatalysts whose pairs are separated by longer energetic range are more photoactive, as recombination is thermodynamically more difficult, increasing recombination time.

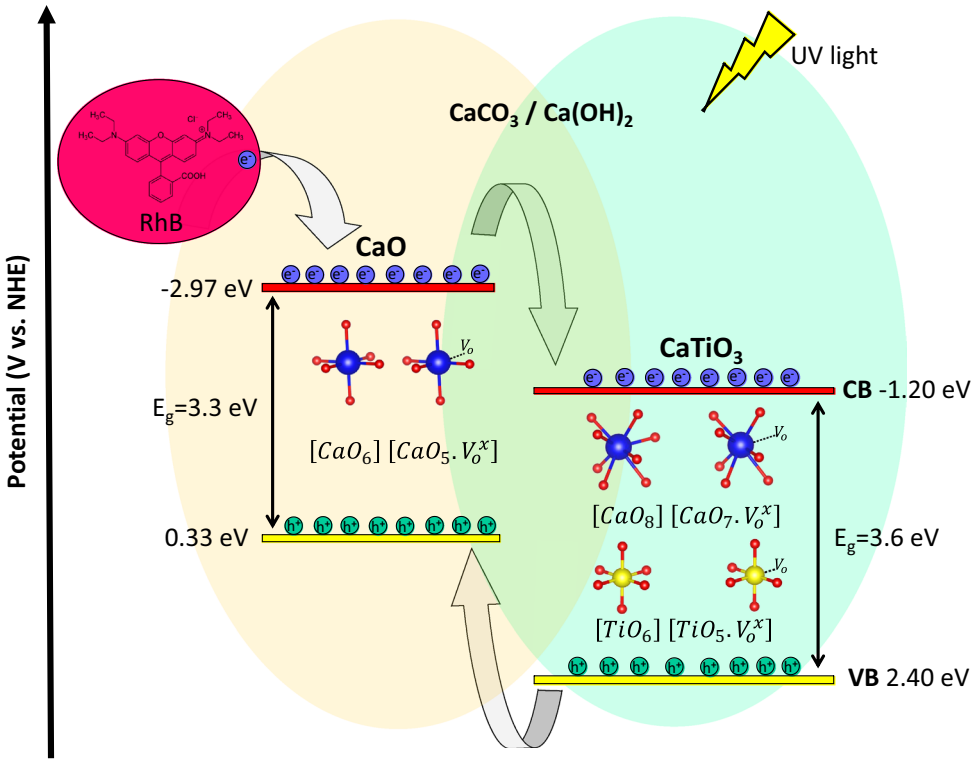

Fig. 11 Scheme showing the conduction and valence bands of the Ca^{2+}-based quaternary heterojunction

Table 6 Photocatalysis data of $CaO/CaTiO_3/CaCO_3/Ca(OH)_2$ heterojunctions and their respective spectral percentages in the green and red region generated by the deconvolution of the photoluminescence spectra

Samples	Discoloration in 120 min (%)	$k \times 10^{-2}$ (min^{-1})	$t_{1/2}$—calculated (min)	Spectra in the region:	
				Green (%)	Red (%)
Ca + 0.25%CTO	90.1	1.799	38.5	92.91	7.09
Ca + 0.5%CTO	89.5	1.793	38.7	91.92	8.08
Ca + 2%CTO	86.8	1.530	45.3	79.23	20.77
Ca + 10%CTO	86.0	1.514	45.8	62.64	37.36
Ca + 50%CTO	41.2	0.395	175.5	35.73	64.27

4 Conclusion

Quaternary heterojunctions—$CaO/CaTiO_3/CaCO_3/Ca(OH)_2$—were obtained. Crystalline structure, optical properties, and defects generated in the formation of the heterojunctions were correlated with the photocatalytic process. The increasing $CaTiO_3$ content in the heterojunction reduced the band gap energy and changed the photoluminescent emission energy according to the dielectric and titanate phases present. Heterojunction with the lowest $CaTiO_3$ concentration and better photocatalytic activity was found to present intense energy emission in the region related to defects in the double-ionized oxygen vacancy. The chemical environment was evaluated and it was proved that the observed emission in the PL spectra was related to defects in relation to the oxygen ions, and there was no alteration of the oxidation state of the metal ions. The RhB photodiscoloration study using scavengers showed that the most photoactive species among the Ca-based catalysts were superoxide radicals ($O_2^{\cdot-}$). The stability and reuse of the heterojunction were evaluated, showing good performance. There was similarity in the photoactive species generated in the heterojunction and in the pure materials; however, it was demonstrated that the former presented a different energy decay region, which favored the charge separation process.

Acknowledgments This work was supported by the São Paulo Research Foundation (Grant CEPID/CDMF—FAPESP: 2013/07296-2 and 2017/19143-7) and the National Council for Scientific and Technological Development (CNPq). We are also grateful the LMA-IQ for providing the FEG-SEM facilities.

Compliance with ethical standard

Conflict of interest On behalf of all authors, the corresponding author states that there is no conflict of interest.

References

1. Ma Z, Xiao Z, Zhou WY, Jin LF, Huang DJ, Jiang HF, Yang T, Liu YC, Huang YL (2020) Efficient $CH_3NH_3PbI_{3-x}(SeCN)_x$ perovskite solar cells with improved crystallization and defect passivation. J Alloy Compd 822:153539
2. Ding Y, Chen J, Chen H, Yang YM, Xu J, Yao JX (2020) Atmosphere dependent gas-solid reaction for high-quality $MAPbBr_3$ perovskite solar cells. Appl Surf Sci 510:145356
3. Senol SD, Ozugurlu E, Arda L (2020) Synthesis, structure and optical properties of (Mn/Cu) co-doped ZnO nanoparticles. J Alloy Compd 822:153514
4. Alasvand A, Kafashan H (2020) Investigation the effect of Pb incorporation on the surface characterizations of electrodeposited CdSe nanostructures. J Alloy Compd 817:152711
5. Zhao XW, Yang Z, Guo JT, Hu GC, Yue WW, Yuan XB, Ren JF (2020) Enhanced valley polarization at valence/conduction band in transition-metal-doped WTe_2 under strain force. Sci Rep 10:4028
6. Han C, Jing MX, Yang H, Shen XQ, Qiao GJ (2019) An overlapped nano-Fe_2O_3/TiO_2 composite coating on activated carbon fiber membrane with enhanced photocatalytic performance. J Nanosci Nanotechnol 19(11):7123–7130
7. Liu C, Dong SS, Chen YG (2019) Enhancement of visible-light-driven photocatalytic activity of carbon plane/g-C_3N_4/TiO_2 nanocomposite by improving heterojunction contact. Chem Eng J 371:706–718
8. Naraginti S, Yu YY, Fang Z, Yong YC (2019) Novel tetrahedral Ag_3PO_4@N-rGO for photocatalytic detoxification of sulfamethoxazole: process optimization, transformation pathways and biotoxicity assessment. Chem Eng J 375:11
9. Amoresi RAC, Teodoro V, Teixeira GF, Li MS, Simoes AZ, Perazolli LA, Longo E, Zaghete MA (2018) Electrosteric colloidal stabilization for obtaining $SrTiO_3/TiO_2$ heterojunction: microstructural evolution in the interface and photonics properties. J Eur Ceram Soc 38(4):1621–1631
10. Coleto U, Amoresi RAC, Teodoro V, Iani IM, Longo E, Zaghete MA, Perazolli LA (2018) An approach for photodegradation mechanism at $TiO_2/SrTiO_3$ interface. J Mater Sci Mater Electron 29(23):20329–20338
11. Coleto U, Amoresi RAC, Pereira CAM, Simoes AZ, Zaghete MA, Monteiro ES, Longo E, Perazolli LA (2019) Influence of defects on photoluminescent and photocatalytic behavior of $CaO/SrTiO_3$ heterojunctions. Ceram Int 45(12):15244–15251
12. Ge SX, Li DP, Cui ZK, Zhang YK, Zhang S, Zhang TY, Jia GY, He WW, Zheng Z (2019) Regulating the relative content of $^{\cdot}O^{2-}$ and $^{\cdot}OH$ for PCPNa degradation on BiOCl plates with controllable exposed crystal faces and surface oxygen vacancies. Sep Purif Technol 228:115743
13. Sahu BK, Das A, Prasad AK, Mangamma G (2019) The role of in-plane oxygen vacancy defects in SnO_2 nanoparticles for CH_4 sensing. J Nanosci Nanotechnol 19(12):7764–7770
14. Rong QY, Zhang DP, Li Y, Zha ZX, Geng XX, Cui SH, Yang J (2019) Synthesis of $Bi_2MoO_6/Bi_2Ti_2O_7$ Z-scheme heterojunction as efficient visible-light photocatalyst for the glycolic acid degradation. J Nanosci Nanotechnol 19(12):7635–7644
15. Yuan X, Yu LM, Ma HN, Li Y, Li C, Yin ML, Du HB, Hui FX (2019) Direct synthesis of upstanding graphene/ZnO nanowalls/graphene sandwich heterojunction and its application for NO_2 gas sensor. J Nanosci Nanotechnol 19(12):7947–7952
16. Freitas DG, Iani IM, Amoresi RAC, Coletto UJ, Pereira CAM, Simões AZ, Perazolli LA, Zaghete MA (2019) Structural and morphological characterization of the $SrTiO_3/TiO_2$ heterojunction obtained by chemical method. In: Aguilera JG, Zuffo AM (eds) Ciências Exatas e da Terra e a Dimensão Adquirida através da Evolução Tecnológica. Atena Editora, Ponta Grossa, pp 93–105
17. Wang XF, Yu JC, Fu C, Li TY, Yu HG (2019) Self-templated formation of $AgCl/TiO_2$ hollow octahedra for improved visible-light photocatalytic activity. Appl Surf Sci 494:740–748
18. Yang YL, Zhang DN, Xiang QJ (2019) Plasma-modified $Ti_3C_2T_x$/CdS hybrids with oxygen-containing groups for high-efficiency photocatalytic hydrogen production. Nanoscale 11(40):18797–18805
19. Chen D, Liu ZF, Zhang SC (2020) Enhanced PEC performance of hematite photoanode coupled with bimetallic oxyhydroxide NiFeOOH through a simple electroless method. Appl Catal B Environ 265:118580
20. Wang MS, Fu WY, Du L, Wei YS, Rao P, Wei L, Zhao XS, Wang Y, Sun SH (2020) Surface engineering by doping manganese into cobalt phosphide towards highly efficient bifunctional HER and OER electrocatalysis. Appl Surf Sci 515:146059
21. Zhang SC, Liu ZF, Chen D, Guo ZG, Ruan MN (2020) Oxygen vacancies engineering in TiO_2 homojunction/ZnFe-LDH for enhanced photoelectrochemical water oxidation. Chem Eng 395:125101
22. Sanchez-Cantu M, Peralta MDR, Galindo-Rodriguez AB, Puente-Lopez E, Rubio-Rosas E, Gomez CM, Tzompantzi F (2017) Calcium-containing materials as alternative catalysts in advanced oxidation process. Fuel 198:76–81
23. Osuntokun J, Onwudiwe DC, Ebenso EE (2018) Aqueous extract of broccoli mediated synthesis of CaO nanoparticles and its application in the photocatalytic degradation of bromocrescol green. IET Nanobiotechnol 12(7):888–894
24. Peralta MDR, Sanchez-Cantu M, Puente-Lopez E, Rubio-Rosas E, Tzompantzi F (2018) Evaluation of calcium oxide in Rhodamine 6G photodegradation. Catal Today 305:75–81
25. Bathla A, Singla D, Pal B (2019) Highly efficient $CaCO_3$-CaO extracted from tap water distillation for effective adsorption and photocatalytic degradation of malachite green dye. Mater Res Bull 116:1–7
26. Furusawa T, Watanabe M, Kadota R, Matsumoto T, Sato M, Suzuki N (2015) Methanolysis of rapeseed oil to fatty acid methyl esters using microencapsulated CaO and TiO_2-supported chromium oxide under light irradiation. Fuel Process Technol 140:125–131
27. Raizada P, Priya B, Thakur P, Singh P (2016) Solar light induced photodegradation of oxytetracyline using Zr doped TiO_2/CaO based nanocomposite. Indian J Chem A 55(7):803–809
28. Abbas SJ, Ramacharyulu P, Lo HH, Ali SI, Ke SC (2017) A catalytic approach to synthesis of PLP analogs and other environmental protocols in a single handed CaO/TiO_2 green nanoparticle. Appl Catal B Environ 210:276–289
29. Mohamad M, Ngadi N, Wong SL, Jusoh M, Yahya NY (2017) Prediction of biodiesel yield during transesterification process using response surface methodology. Fuel 190:104–112
30. Ghazali SS, Kem WL, Jusoh R, Abdullah S, Shariffuddin JH (2019) Evaluation of La-doped CaO derived from cockle shells for photodegradation of POME. Bull Chem React Eng Catal 14(1):205–218
31. Shaveisi Y, Sharifnia S (2018) Deriving Ag_3PO_4-CaO composite as a stable and solar light photocatalyst for efficient ammonia degradation from wastewater. J Energy Chem 27(1):290–299
32. Meng L, Zhang KF, Pan K, Qu Y, Wang GF (2016) Controlled synthesis of $CaTiO_3:Ln^{3+}$ nanocrystals for luminescence and photocatalytic hydrogen production. RSC Adv 6(7):5761–5766

33. Shi R, Waterhouse GIN, Zhang TR (2017) Recent progress in photocatalytic co_2 reduction over perovskite oxides. Solar Rrl 1(11):17
34. Yan YX, Yang H, Yi Z, Li RS, Wang XX (2019) Enhanced photocatalytic performance and mechanism of Au@$CaTio_3$ composites with au nanoparticles assembled on $CaTio_3$ nanocuboids. Micromachines 10(4):254
35. Park BG (2019) Photoluminescence of Eu^{3+}-doped $CaTiO_3$ perovskites and their photocatalytic properties with a metal ion loading. Chem Phys Lett 722:44–49
36. Lin JJ, Hu JS, Qiu CW, Huang HJ, Chen L, Xie YY, Zhang ZZ, Lin HX, Wang XX (2019) In situ hydrothermal etching fabrication of $CaTiO_3$ on TiO_2 nanosheets with heterojunction effects to enhance CO_2 adsorption and photocatalytic reduction. Catal Sci Technol 9(2):336–346
37. Han JS, Liu Y, Dai FX, Zhao RY (2018) Wang L (2018) Fabrication of CdSe/$CaTiO_3$ nanocomposties in aqueous solution for improved photocatalytic hydrogen production. Appl Surf Sci 459:520–526
38. Pan JQ, Jiang ZY, Feng SX, Zhao C, Dong ZJ, Wang BB, Wang JJ, Song CS, Zheng YY, Li C (2018) The enhanced photocatalytic hydrogen production of the fusiform g-C_3N_4 modification $CaTiO_3$ nano-heterojunction. Int J Hydrogen Energy 43(41):19019–19028
39. Su TM, Qin ZZ, Ji HB, Wu ZL (2019) An overview of photocatalysis facilitated by 2D heterojunctions. Nanotechnology 30(50):502002
40. Naeemullah, Murtaza G, Khenata R, Safeer A, Alahmed ZA, Bin Omran S (2014) Shift of band gap from indirect to direct and optical response of CaO by doping S, Se, Te. Comput Mater Sci 91:43–49
41. Tariq S, Ahmed A, Saad S (2015) Structural, electronic and elastic properties of the cubic $CaTiO_3$ under pressure: a DFT study. AIP Adv 5(7):077111
42. Kurkcu C, Merdan Z, Yamcicier C (2018) Structural phase transition and electronic properties of CaO under high pressure. Mater Res Express 5(12):9
43. Longo VM, de Figueiredo AT, de Lazaro S, Gurgel MF, Costa MGS, Paiva-Santos CO, Varela JA, Longo E, Mastelaro VR, De Vicente FS, Hernandes AC, Franco RWA (2008) Structural conditions that leads to photoluminescence emission in $SrTiO_3$: an experimental and theoretical approach. J Appl Phys 104(2):023515
44. Lei Y, Zhang LD, Meng GW, Li GH, Zhang XY, Liang CH, Chen W, Wang SX (2001) Preparation and photoluminescence of highly ordered TiO_2 nanowire arrays. Appl Phys Lett 78(8):1125–1127
45. Pan XY, Yang MQ, Fu XZ, Zhang N, Xu YJ (2013) Defective TiO_2 with oxygen vacancies: synthesis, properties and photocatalytic applications. Nanoscale 5(9):3601–3614
46. Wu JM, Shih HC, Wu WT, Tseng YK, Chen IC (2005) Thermal evaporation growth and the luminescence property of TiO_2 nanowires. J Cryst Growth 281(2–4):384–390
47. Zhang YJ, Wang J, Sahoo MPK, Shimada T, Kitamura T (2015) Mechanical control of magnetism in oxygen deficient perovskite $SrTiO_3$. Phys Chem Chem Phys 17(40):27136–27144
48. Ni M, Ratner BD (2008) Differentiating calcium carbonate polymorphs by surface analysis techniques: an XPS and TOF-SIMS study. Surf Interface Anal 40(10):1356–1361
49. Yaseen SA, Yiseen GA, Li ZJ (2018) Synthesis of calcium carbonate in alkali solution based on graphene oxide and reduced graphene oxide. J Solid State Chem 262:127–134
50. Wang JH, Wei YW, Li N, Chen JF (2019) Hydration resistance of CaO material prepared by $Ca(OH)_2$ calcination with chelating compound. Materials 12(14):2325
51. Sugama T, Kukacka LE, Carciello N, Hocker NJ (1989) Study of interactions at water-soluble polymer $Ca(OH)_2$ or gibbsite interfaces by XPS. Cement Concrete Res 19(6):857–867
52. Jilani A, Iqbal J, Abdel-Wahab MS, Jamil Y, Al-Ghamdi AA (2016) X-ray photoelectron spectroscopic (XPS) investigation of interface diffusion of ZnO/Cu/ZnO multilayer. J Optoelectron Adv Mater 8(1):27–31
53. Smyth CM, Addou R, McDonnell S, Hinkle CL, Wallace RM (2017) WSe_2-contact metal interface chemistry and band alignment under high vacuum and ultra high vacuum deposition conditions. 2D Mater 4(2):025084
54. Zhu CQ, Li CL, Zheng MJ, Delaunay JJ (2015) Plasma-induced oxygen vacancies in ultrathin hematite nanoflakes promoting photoelectrochemical water oxidation. ACS Appl Mater Interfaces 7(40):22355–22363
55. Liu MY, Zheng YF, Song XC (2020) One-pot facile synthesis of $AgIO_3$/Ag_2O/Ag nanocomposites with enhanced photocatalytic activity. J Nanosci Nanotechnol 20(2):802–809
56. Fujishima A, Zhang XT, Tryk DA (2008) TiO_2 photocatalysis and related surface phenomena. Surf Sci Rep 63(12):515–582
57. Bekena FT, Abdullah H, Kuo DH, Zeleke MA (2019) Photocatalytic reduction of 4-nitrophenol using effective hole scavenger over novel Mg-doped Zn(O, S) nanoparticles. J Ind Eng Chem 78:116–124
58. Vattikuti SVP, Devarayapalli KC, Nagajyothi PC, Shim J (2019) Binder-free WS_2/ZrO_2 hybrid as a photocatalyst for organic pollutant degradation under UV/simulated sunlight and tests for H_2 evolution. J Alloy Compd 809:14
59. Sharma B, Mukhopadhyay A, Banerjee L, Sengupta A, Rahaman H, Sarkar CK (2019) Ab initio study of mono-layer 2-D insulators (X-$(OH)_2$ and h-BN) and their use in MTJ memory device. Microsyst Technol 25(5):1909–1917
60. Zhang QP, Zhu WF, Liang DM, Wu XL, Chen RC, Sun N, Li YT, Zhou YL (2019) Core-shell structured $CaCO_3$@CNF for enhanced dielectric properties of polymer nanocomposites. Appl Surf Sci 487:77–81
61. Pei JY, Meng J, Wu SY, Lin QY, Wei X, Li JX, Zhang Z (2020) Effects of Ca/Ti ratio on morphology control and photocatalytic activity of $CaTiO_3$/$Ca(OH)_2$ composite photocatalyst. Mater Lett 276:128229
62. Mousavi M, Habibi-Yangjeh A, Abitorabi M (2016) Fabrication of novel magnetically separable nanocomposites using graphitic carbon nitride, silver phosphate and silver chloride and their applications in photocatalytic removal of different pollutants using visible-light irradiation. J Colloid Interf Sci 480:218–231
63. Tang HJ, Duan YF, Zhu C, Cai TY, Li CF, Cai L (2017) Theoretical evaluation on selective adsorption characteristics of alkali metal-based sorbents for gaseous oxidized mercury. Chemosphere 184:711–719
64. Yan X, Huang XJ, Fang Y, Min YH, Wu ZJ, Li WS, Yuan JM, Tan LG (2014) Synthesis of rodlike $CaTiO_3$ with enhanced charge separation efficiency and high photocatalytic activity. Int J Electrochem Sci 9(9):5155–5163